URSI GASS 2020, Rome, Italy, 29 August - 5 September 2020

3D-Printed Microwave Encoders based on Embedded and Buried Dielectric Inclusions

C. Herrojo, F. Paredes*, and F. Martín
CIMITEC, Departament d'Enginyeria Electrònica, Universitat Autònoma de Barcelona, 08193 Bellaterra, Spain

Abstract

In this paper, 3D-printed permittivity contrast microwave encoders based on embedded and buried dielectric inclusions are presented. The inclusions, made of a high, or low, dielectric constant material as compared to the one of the host substrate, are square shaped, so that they can be easily detected by means of a dedicated reader based on a permittivity sensor. By embedding the inclusions in the host substrate during encoder fabrication, rather than printing them on top of it, we avoid protuberances that may jeopardize encoder robustness against mechanical wearing (i.e., friction). Moreover, it is demonstrated that encoder functionality is preserved by burying the inclusions in the host substrate. By this means, the inclusions are not visible, and this provides system security for identification applications. The proposed encoders are also useful for the measurement of linear displacements and velocities.

1 Introduction

Recently, all-dielectric microwave encoders based on chains of apertures made in a dielectric substrate have been reported [1]. Encoder reading is based on the permittivity contrast between the apertures and the host substrate. Thus, by means of a dedicated reader based on a sensor able to locally detect changes in the permittivity of the surrounding medium, the apertures can be detected. In [1, 2], a microstrip line loaded with a complementary spiral resonator (CSR) [3] was used as sensitive element of the reader. The reason is that, through encoder motion over the reader (as required in a reading operation), the frequency response of the CSR-loaded line experiences significant changes when the apertures are located on top of the CSR. Consequently, by feeding the line with a harmonic (interrogation) signal conveniently tuned, an amplitude modulated (AM) signal is generated at the output port of the CSR-loaded line. The envelope function of such signal contains the relevant information related to the encoder, i.e., the identification (ID) code (provided only a subset of apertures is present in the predefined positions of the chain). If all the apertures are present, the relative displacement and instantaneous velocity between the reader and the encoder is given by the cumulative number of peaks, or dips, in the envelope function, and by the distance between adjacent peaks, or dips, respectively.
These all-dielectric encoders constitute a good alternative to optical encoders [4]-[6] in applications where low-cost, rather than encoder resolution, is the primary goal. It should be also mentioned that all-dielectric encoders may offer major levels of robustness under operation in harsh environments (i.e., extreme temperatures, polluted ambient, radiation, etc.).
Electromagnetic encoders based on chains of metallic elements printed or etched on a dielectric substrate (including plastic and paper substrates) have been also recently reported [7]-[11]. Such encoders are very competitive in terms of resolution and data density and capacity (e.g., in [11], the functionality of 80-bit inkjet-printed electromagnetic encoders, or tags, implemented on ordinary paper was demonstrated). However, such encoders are more sensitive to wearing and aging effects as compared to all-dielectric encoders. Particularly, unexpected metal cuts caused, e.g., by mechanical friction, can be interpreted by the reader as a variation of the ID code (indeed, it was demonstrated in [10] that tag programming by cutting the required printed elements of the chain is possible).
In this paper, we report all-dielectric permittivity contrast electromagnetic encoders, conceptually similar to those reported in [1]. However, the encoders of this paper are manufactured by a full 3D-printing process. Such process allows for the implementation of dielectric inclusions (not only apertures) either embedded or buried in the host substrate. In both cases, the encoders are extremely robust against mechanical wearing or aging. Moreover, the encoders based on buried inclusions obscure the identification by direct sight, thereby proving further levels of confidence against copy or plagiarism.

2 The 3D-Printing Process and Materials

The encoders have been manufactured by means of the *Ultimaker* 3 Extended 3D printer. This 3D-printer is based on fused filament fabrication (FFF) technology, i.e., a 3D-printing process that uses a continuous filament of a thermoplastic material. The maximum resolution of this 3D-printer in *x*-, *y*-, and *z*-directions is 12.5 μm, 12.5 μm, and 2.5 μm, respectively, which is enough for our purposes. The considered filaments for encoder fabrication are *PLA Polylactic acid* and *RS Pro MT-Copper*. The use of such materials is justified by the significant contrast of their respective dielectric constants. Indeed, before the selection of such specific materials, determination of their dielectric constants and loss tangents was carried out. For that purpose, square samples of 60 mm side length with a thickness of 1 mm were 3D-printed with both types of filaments. Such dimensions are

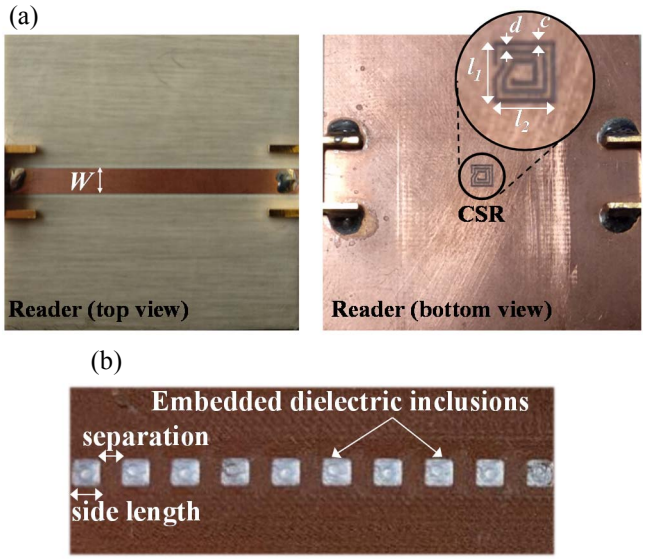

Figure 1. Photograph of the sensitive part of the reader (a) and encoder with embedded low dielectric constant inclusions (b). The thickness of the encoders is 1 mm. The thickness of the reader substrate is 1.52 mm and the dielectric constant is ε_r = 3.55. Dimensions of the sensitive part of the reader (in mm) are: W = 3.43, L = 10, l_1 = l_2 = 2.80, and c = d = 0.20. Dimensions of the embedded square dielectric inclusions (in mm) are: 2.8 mm side length and 2.4 mm separation.

those recommended in the datasheet of the resonant cavity *Agilent 85072A*, used for the measurement of the dielectric constant and loss tangent. For *PLA Polylactic acid* the measured results were found to be ε_r = 3 and tanδ = 0.010, whereas ε_r = 7.6 and tanδ = 0.015 were obtained for *RS Pro MT-Copper*. The dielectric permittivity contrast between both materials (defined as the dielectric constants ratio) is not as good as the one between vacuum (apertures) and the considered encoder substrate in [1] (the *Rogers RO4003C* with ε_r = 3.55 and tanδ = 0.0021). Nevertheless, it will be show next that such combination of materials is adequate for the implementation of the intended encoders, which will be read by means of a reader identical the one reported in [1].

3 Reader and Encoder Design

The sensitive part of the reader is a microstrip line loaded with a complementary spiral resonator (CSR), identical to the one reported in [1]. The dimensions of the apertures in the encoders reported in that paper were optimized for encoder reading. Thus, in this paper, the same dimensions for the dielectric inclusions, either embedded or buried, will be considered. By this means, we do expect that the encoders can be correctly read, despite the fact that the dielectric contrast of the 3D-printing materials is not as good as in [1]. Figure 1 shows the photograph of the fabricated reader (implemented on the *Rogers RO4003C* substrate by means of a *LPKF-H100* milling machine), as well as the photograph of one of the 3D-printed encoders, i.e., the one with embedded inclusions. In these full 3D-printed encoders, the low and high dielectric constant filaments are applied to the inclusions and to the host substrate, respectively.

As mentioned before, encoders with buried high dielectric constant inclusions are also considered (picture is not shown since the inclusions are not visible). In this case, the thickness of the inclusions is 1 mm, whereas the (estimated) thickness of the host substrate at both sides of the inclusions is 0.1 mm (the side length of the square inclusions is the one indicated in the caption of Fig. 1 for the embedded inclusions).

4 Experimental Validation

Encoder reading has been carried out by means of the experimental setup available in our laboratory, consisting of a function generator (model *Agilent E44338C*), used for the generation of the harmonic (interrogation) signal, and an envelope detector (that provides the envelope function). An isolator (based on the *ATM ATc4-8* circulator) is cascaded between the envelope detector and the output port of the sensing line, in order to avoid reflections from the diode, a high nonlinear device. The envelope detector is implemented by means of the Avago *HSMS-2860* diode and the active probe *N2795A*, connected to an oscilloscope (model *Agilent MSO-X-3104A*), where the envelope function is visualized. Finally, encoder motion over the reader has been carried out by means of a linear displacement system (model *STM 23Q-3AN*), which allows for an accurate control of the encoder position in three dimensions, as well as encoder velocity.

4.1 Encoders based on Embedded Dielectric Inclusions

We have considered two different 10-bit encoders with embedded inclusions; one of them with all the inclusions 3D-printed at the predefined positions in the chain (corresponding to the bit sequence '111…'); the other one with the presence and absence of dielectric inclusions alternating (corresponding to the ID code '1010…'). Figure 2 depicts the measured envelope functions for both encoders (their photographs are included as insets). From these results, it can be concluded that the reader is able to correctly provide the corresponding codes. Moreover, the relative velocity between the encoder and the reader can be inferred from the distance between adjacent peaks, or dips, in the envelope function, provided a periodic sequence of inclusions in the chain is considered. From the graphs of Fig. 2, with peaks separated a time lapse of 1.0345 s and 0.5283 s, as indicated, the resulting instantaneous velocities are found to be 1.005 cm/s and 0.984 cm/s, respectively, i.e, very close to the nominal value (1 cm/s). The nominal air gap (or vertical distance between the encoder and the reader) has been set to 0.1 mm.

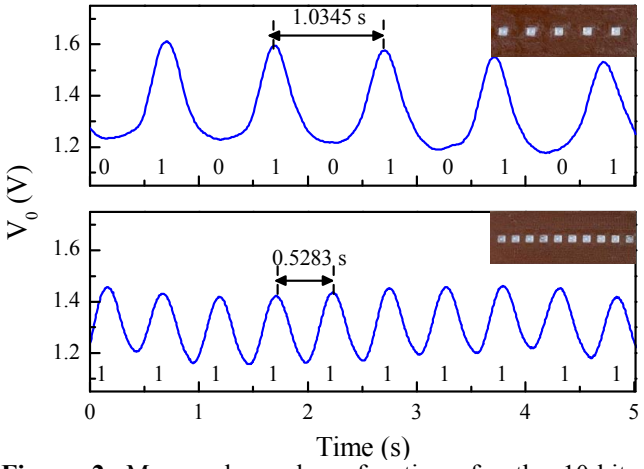

Figure 2. Measured envelope functions for the 10-bit encoders based on embedded inclusions depicted in the inset, with ID codes '1010101010' (a) and '1111111111' (b).

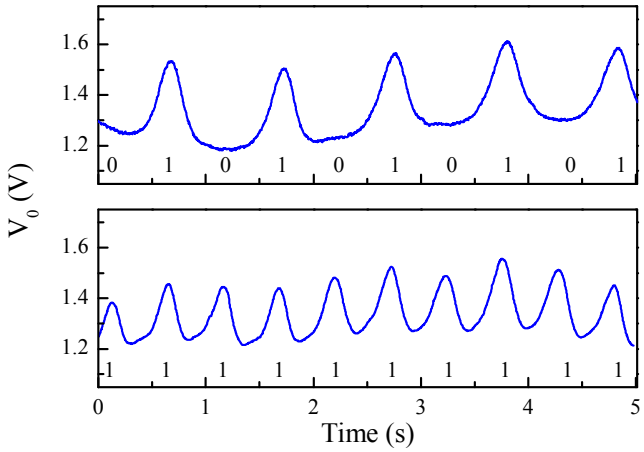

Figure 3. Measured envelope functions for the 10-bit encoders based on buried inclusions, with ID codes '1010101010' (a) and '1111111111' (b).

4.2 Encoders based on Buried Dielectric Inclusions

For the encoders with buried 3D-printed inclusions, we have considered the same bit sequences. The measured envelope functions are depicted in Fig. 3, where it can be seen that the ID codes of these buried encoders are also correctly predicted. Therefore, the functionality of all-dielectric 3D-printed encoders with invisible (buried) inclusions is demonstrated. Encoder manufacturing with obscured bit sequence is an interesting aspect for chipless-RFID applications, as far as the ID code can only be determined by a dedicated reader. Therefore, the system provides a major level of confidence against copying, spying, or plagiarism, as compared to other identification/authentication systems that use electromagnetic encoders based on visible patterns [1],[9]-[11], either implemented as dielectric or metallic inclusions. Similar to electromagnetic encoders based on metallic inclusions, the achievable number of bits of these all-dielectric 3D-printed encoders is only limited by tag size. This represents an advantage over traditional chipless-RFID systems based on time domain reflectometry [12]-[16] or based on the spectral signature [17]-[21].

5 Conclusions

In conclusion, full 3D-printed electromagnetic encoders based on permittivity contrast have been presented. These encoders are implemented by means of chains of 3D-printed low dielectric constant inclusions embedded or buried in a host substrate with high dielectric constant, also 3D-printed. For encoder reading, a dedicated reader based on a CSR loaded microstrip line, fed by a harmonic signal, has been used. Such resonant element is very sensitive to permittivity changes in its surrounding medium. Therefore, the CSR has been found to be a convenient element to detect the presence of inclusions at their predefined position. The presence of such inclusions is revealed by peaks, or dips, in the envelope function of the amplitude modulated (AM) signal generated by encoder motion over the reader. Encoder reading has been experimentally validated for both types of encoders. By embedding and burying the inclusions in the host substrate, the encoders are very robust against mechanical friction. Moreover, the encoders based on buried inclusions offer high levels of confidence against copying or spying, as far as the inclusions are not visible.

6 Acknowledgements

This work was supported by MINECO-Spain under Project TEC2016-75650-R, by Generalitat de Catalunya under project 2017SGR-1159, by the Institució Catalana de Recerca i Estudis Avançats (who awarded Ferran Martín), and by FEDER funds.

7 References

1. C. Herrojo, F. Paredes, J. Mata-Contreras, F. Martín, "All-dielectric electromagnetic encoders based on permittivity contrast for displacement/velocity sensors and chipless-RFID tags", *IEEE-MTT-S Int. Microw. Symp*. (IMS'19), Boston (MA), USA, Jun. 2019.

2. C. Herrojo, F. Paredes, P. Vélez and F. Martin, "Microwave Encoders and Application to Near-Field Chipless-RFID: a Review," *2019 IEEE-APS Topical Conference on Antennas and Propagation in Wireless Communications (APWC)*, Granada, Spain, 2019, pp. 21-25.

3. J. Selga, G. Sisó, M. Gil, J. Bonache and F. Martín, "Microwave circuit miniaturization with complementary spiral resonators (CSRs): application to high-pass filters and dual-band components", *Microw. Opt. Technol. Lett.*, **51**, Nov. 2009, pp. 2741-2745.

4. E. Eitel, "Basics of rotary encoders: overview and new technologies", *Machine Design Magazine*, 7 May 2014.

5. G. K. McMillan, D.M. Considine, Eds., *Process Instruments and Controls Handbook*, Fifth Edition, McGraw Hill 1999, ISBN 978-0-07-012582-7, page 5.26.

6. X. Li, J. Qi, Q. Zhang, and Y. Zhang, “Bias-tunable dual-mode ultraviolet photodetectors for photoelectric tachometer,” *Appl. Phys. Lett*., **104**, 4, Jan. 2014, pp. 041108-1–041108-4.

7. J. Mata-Contreras, C. Herrojo, and F. Martín, “Application of split ring resonator (SRR) loaded transmission lines to the design of angular displacement and velocity sensors for space applications”, *IEEE Trans. Microw. Theory Techn.*, **65**, 11, Nov. 2017, pp. 4450-4460.

8. C. Herrojo, J. Mata-Contreras, F. Paredes, F. Martín, “Microwave encoders for chipless RFID and angular velocity sensors based on S-shaped split ring resonators (S-SRRs)”, *IEEE Sensors J*., **17**, Aug. 2017, pp. 4805-4813.

9. C. Herrojo, J. Mata-Contreras, F. Paredes, Ferran Martín, “Near-field chipless RFID system with high data capacity for security and authentication applications”, *IEEE Trans. Microw. Theory Techn*., **65**, 12, Dec. 2017, pp. 5298-5308.

10. C. Herrojo, J. Mata-Contreras, F. Paredes, A. Núñez, E. Ramon, and F. Martín, “Near-field chipless-RFID system with erasable/programmable 40-bit tags inkjet printed on paper substrates”, *IEEE Microw. Wireless Compon. Lett.*, **28**, Mar. 2018, pp. 272-274.

11. C. Herrojo, M. Moras, F. Paredes, A. Núñez, E. Ramón, J. Mata-Contreras, F. Martín, “Very low-cost 80-bit chipless-RFID tags inkjet printed on ordinary paper”, *Technologies*, **6**, p. 52, 2018; doi:10.3390/technologies6020052.

12. A. Chamarti and K. Varahramyan, "Transmission delay line based ID generation circuit for RFID applications," *IEEE Microw. Wireless Compon. Lett.*, **16**, pp. 588-590, 2006.

13. M. Schüßler, C. Damm, M. Maasch, and R. Jakoby, “Performance evaluation of left-handed delay lines for RFID backscatter applications,” *IEEE MTT-S Int. Microw. Symp. 2008*, pp. 177-180.

14. F.J. Herraiz-Martínez, F. Paredes, G. Zamora, F. Martín, and J. Bonache, “Printed magnetoinductive-wave (MIW) delay lines for chipless RFID applications”, *IEEE Trans. Ant. Propag.*, **60**, Nov. 2012, pp. 5075-5082.

15. R. Nair, E. Perret, and S. Tedjini, “Temporal multi-frequency encoding technique for chipless RFID applications,” *IEEE MTT-S Int. Microw. Symp.*, Montreal, Canada, Jun. 2012, pp. 1–3.

16. S. Gupta, B. Nikfal, and C. Caloz, “Chipless RFID system based on group delay engineered dispersive delay structures,” *IEEE Ant. Wirel. Propag. Lett*., **10**, 2, Dec. 2011, pp. 1366–1368.

17. S. Preradovic, I. Balbin, N. C. Karmakar, and G. F. Swiegers, "Multiresonator-based chipless RFID system for low-cost item tracking," *IEEE Trans. Microw. Theory Techn.*, **57**, May 2009, pp. 1411-1419.

18. S. Preradovic and N. C. Karmakar, "Design of chipless RFID tag for operation on flexible laminates," *IEEE Anten. Wireless Propag. Lett.*, **9**, pp. 207-210, 2010.

19. A. Vena, E. Perret, and S. Tedjini, “High-capacity chipless RFID tag insensitive to the polarization”, *IEEE Trans. Ant. Propag.*, **60**, 10, Oct. 2012, pp. 4509-4515.

20. S. Genovesi, F. Costa, A. Monorchio, G. Manara, “Chipless RFID tag exploiting multifrequency delta-phase quantization encoding”, *IEEE Ant. Wireless, Propag. Lett*., **15**, pp. 738-741, 2015.

21. A. Vena, E. Perret, S. Tedjini, "Chipless RFID tag using hybrid coding technique*," IEEE Trans. Microw. Theory Techn*., **59**, Dec. 2011, pp. 3356-3364.